Biotic responses to volatile volcanism and environmental stresses over the Guadalupian-Lopingian (Permian) transition.

Article:

Huang, Y, Chen, ZQ, Wignall, PB et al. (4 more authors) (2019) Biotic responses to volatile volcanism and environmental stresses over the Guadalupian-Lopingian (Permian) transition. Geology, 47 (2). pp. 175-178. ISSN 0091-7613

https://doi.org/10.1130/G45283.1

Publisher: GSA
Journal: GEOL: Geology
DOI:10.1130/G45283.1

Biotic responses to volatile volcanism and environmental stresses over Guadalupian-Lopingian (Permian) transition

Yuangeng Huang[1], Zhong-Qiang Chen[1]*, Paul B. Wignall[2], Stephen E. Grasby[3], Laishi Zhao[4], Xiangdong Wang[4], and Kunio Kaiho[5]

[1]State Key Laboratory of Biogeology and Environmental Geology, China University of Geosciences, Wuhan 430074, China

[2]School of Earth and Environment, University of Leeds, Leeds LS2 9JT, UK

[3]Geological Survey of Canada, Calgary AB T2L-2A7, Canada

[4]State Key Laboratory of Geological Processes and Resource Geology, China University of Geosciences, Wuhan 430074, China

[5]Institute of Paleontology and Geology, Tohoku University, Sendai, Japan

*E-mail: zhong.qiang.chen@cug.edu.cn

ABSTRACT

Biotic extinction during the Guadalupian–Lopingian (G–L) transition is actively debated, with its timing, validity, and causality all questioned. Here we show, based on detailed sedimentary, paleoecologic, and geochemical analyses of the Penglaitan section in South China, that this intra-Permian biotic crisis began with the demise of a metazoan reef system and extinction of corals and alatoconchid bivalves in the late Guadalupian. A second crisis, amongst nektonic organisms occurred around the G-L boundary. Mercury concentration/total organic Carbon (Hg/TOC) ratios show two anomalies. The first

Hg/TOC peak broadly coincided with the reef collapse and a positive shift in Δ^{199}Hg values during a lowstand interval, which was followed by a microbial proliferation. A larger Hg/TOC peak is found just above the G–L boundary and speculatively represents a main eruption episode of Emeishan Large Igneous Province (ELIP). This volatile volcanism coincided with nektonic extinction, a negative $\delta^{13}C_{carb}$ excursion, anoxia, and sea-level rise. The temporal coincidence of these phenomena supports a cause-and-effect relationship, and indicates that the eruption of ELIP likely triggered the G–L crisis.

INTRODUCTION

The fossil record of several major benthic groups from South China reveals a major extinction event around the G–L transition (Jin, 1993; Stanley and Yang, 1994). A contemporaneous biotic crisis has also been recognized in the high-latitude Spitsbergen sections (Bond et al., 2015). However, study of this crisis is hindered by the widespread absence of uppermost Guadalupian and lowermost Lopingian strata due to a major eustatic regression (Haq and Schutter, 2008). Thus, there remains considerable debate about the timing of the extinction: did it occur at the G–L boundary (GLB) or within the Late Guadalupian? Furthermore, the temporal link of the G-L crisis with Emeishan large igneous province (ELIP) suggests that these flood basalt eruptions triggered the crisis (Wignall et al., 2009; Bond et al., 2010).

Here, we examined the G–L succession at the Global Stratotype Section and Point (GSSP) at Penglaitan (PLT) in South China (Fig. 1). This study reports a new metazoan reef, which is investigated alongside a diverse new data set including new carbon isotope values, mercury (Hg) concentrations, and Hg isotopes, that reveal reef collapse and nektonic crisis coincided with extreme environment and volatile volcanism.

GEOLOGICAL SETTING AND METHODS

During the G–L transition, the South China craton was located near the equator in the eastern Paleo-Tethys Ocean (Fig. 1A). Today, the PLT is situated ~20 km southwest of Laibin, Guangxi Province. Here, the Guadalupian strata comprise the Maokou Formation, and the basal Lopingian consists of the Heshan Formation. The G–L strata are subdivided into seven beds (Fig. 1B). Bed 1 is made of siliceous mudstone with chert nodules, and Beds 2–6 have been termed the Laibin Limestone. Beds 2–4 form the major part of a skeletal reef (Fig. 1B), which is capped by bioclastic packstone (Bed 5). Bed 6 is dominantly a crinoidal grainstone while Bed 7 consists of thin-bedded, siliceous mudstone and chert. The GLB is placed at the base of Bed 6k (Fig. 3) and defined by the first occurrence of conodont Clarkina postbitteri postbitteri (Jin et al., 2006).

Fresh rock chips were prepared for microanalysis using a scanning electron microscope to search for microbiota. Rock chips were ground to fine powder using a puck mill for geochemical analysis. $\delta^{13}C_{carb}$ were determined using a Finnigan MAT 251 mass spectrometer, and reported as per mil (‰) relative to Vienna Pee Dee belemnite standard. Volcanism is a major source of Hg to Earth’s surface environments, and the accumulation of Hg in sediment can be used as a proxy indicating ancient volcanism

(Sanei et al., 2012). Hg enrichment is depicted by normalizing to total organic carbon (TOC) due to its high affinity to organic matter. TOC and Hg contents were measured on Elementar vario Macro cube, and LECO AMA254 mercury analyzer, respectively.

Hg isotopes are used to trace the origin and the pathways of the Hg (e.g. Blum and Bergquist., 2007), and their variations are reported in δ^{202}Hg notation referenced to the NIST-3133 Hg standard:

$$\delta^{202}\mathrm{Hg}\ (‰) = [(^{202}\mathrm{Hg}/^{198}\mathrm{Hg}_{\mathrm{sample}})/(^{202}\mathrm{Hg}/^{198}\mathrm{Hg}_{\mathrm{standard}}) -1] \times 1000 \ (1)$$

Mass-independent fractionation (MIF) of Hg isotope is reported in Δ-notation (Δ^{xxx}Hg), describing the difference between the measured δ^{xxx}Hg and the theoretically predicted δ^{xxx}Hg value:

$$\Delta^{xxx}\mathrm{Hg} \approx \delta^{xxx}\mathrm{Hg} - \delta^{202}\mathrm{Hg} \times \beta \ (2)$$

β is equal to 0.2520 for ^{199}Hg, 0.5024 for ^{200}Hg, and 0.7520 for ^{201}Hg (Blum and Bergquist, 2007).

The analytical precision is better than ± 0.1‰ for δ^{13}C, ± 0.2‰ for δ^{18}O, ± 10% for Hg concentration, ± 5% for TOC and ± 0.04‰ for Δ^{199}Hg. Detailed laboratory methods and full data are given in the GSA Data Repository.

RESULTS

Reef Ecosystem Collapse, and Biodiversity Variations near the GLB

Beneath the Laibin Limestone, the Maokou Formation consists of cherty wackestone beds with radiolarians, indicative of a distal ramp to basin setting. A sharp contact is then followed by massive limestones that form a ~25 m wide and ~5 m thick reef (Beds 2–4) (Fig. 1B), with the reef core composed of bryozoan-Tubiphytes framestone (Fig. 2A), coral framestone (Fig. 2C), bryozoan bindstone, and alatoconchid wacke-packstone. The first facies forms the major part of the reef, with in situ bryozoan colonies acting as bafflers and binders. The reef core yields a diverse assemblage of algae, echinoderms, brachiopods, and crinoids encrusted with the bryozoan Fistulipora (Fig. 2B). Alatoconchid shells (Fig. DR1) are another conspicuous component of the reef. The reef is overlain by a cross-stratified grainstone (shoal bank facies; Bed 5) that is in turn capped by a hardground surface. The overlying crinoidal grainstone with Skolithos traces (Fig. DR2), records the persistence of shallow-water following demise of the reef. Bed 7 includes chert and siliceous mudstone, as well as pelagic faunas (ammonoid, sponges, radiolarians), that point to deep-water conditions.

We identified 13 species including small foraminifers (Pachyphloia ovate, Diplosphaerina sp., and Ammodiscus planus), bryozoans (Septopora indet., Fenstella indet., and Fistulipora indet.), corals (Ufimia elongata and Amplexocarinia sp.), giant bivalve (Shikamaia sp.), ammonoid (Pleuronautilus sp.), incertae sedis species (Tubiphytes obscures, Girvanella sp., and Archaeolithoporella sp.). A total of 48 species/indet. species have been obtained from PLT, including: calcareous algae, bivalves, brachiopods, bryozoans, corals, crinoids, echinoids, foraminifera, gastropods, ostracods, sponges and trilobites (Fig. 3). Most (46) species occur in the Laibin Limestone, and only two persisted into the overlying Heshan Formation (Fig. 3). Around half the biodiversity occurs in the reef facies and the remaining taxa, mostly foraminifera occur in Bed 6 while few taxa are recorded by Bed 7 (Fig. 3).

Diverse Microbiota

Microbiota are abundant in the shoal bank facies of the upper Laibin Limestone, including microborings and calcisphere aggregates. Four types of microbe-originated microfossils are identified. Coccoid-like calcispheres (Figs. 2E–F) are comprised of coarse-grained sparitic calcite nuclei coated with thin micritic envelopes, and they are interpreted as endolithic coccoid bacteria (Salama et al., 2015). Bacterial clump-like spheroids (Figs. 2H–I) consisting of dark colored, rounded micritic nuclei surrounded by sparry calcite rims, are consistent with nucleation of bacterial clumps. The problematic microorganism Ovummurus duoportius (Fig. 2G) is made of an ovoid wall, with an internal chamber divided into two equal spaces by a septum-like structure. Microboring Eurygonum nodosum occurs in brachiopod shells (Fig. 2D) and crinoid stems (Fig. 2J), and is thought to be produced by the endolithic cyanobacterium Mastigocoleus testarum (Gektidis et al., 2007).

Sea-level Changes

Sea-level changes associated with a 2nd-order global regression occurs around the G–L transition (Haq and Schutter, 2008) and is well recorded at PLT where a sequence boundary occurs at the basal Laibin Limestone (Wignall et al., 2009). This level is marked by the replacement of deep-water cherty limestones by the reef facies. Water depths continued to shallow and the trend culminates at the top of Bed 5 with the development of a hardground. This was followed by a rapid upward deepening with grainstone shoal facies of Bed 6 overlain by deep-water, finer grained facies of Bed 7 (Fig. 3).

Hg and TOC Concentrations

The strata below the Laibin Limestone comprise chert-rich limestones, and contain low TOC, usually <0.1 wt.%, and Hg concentrations (mostly < 10 ppb) (Fig. DR3). These low Hg values suggest only background levels of volcanic activity. Low TOC values are not suitable for evaluating Hg/TOC (Grasby et al., 2016) below the Laibin Limestone. In contrast, sediments of the Laibin Limestone and Heshan formations have TOC concentrations varying from 0.12 to 2.76 wt.% that are decoupled from variations of Hg concentrations that range up to 26.6 ppb. Hg/TOC ratios fluctuate from 2.1 to 64.1 ppb/wt.% during the Jinogondolella xuanhanensis Zone to lowermost C. postbitteri postbitteri Zone, with a minor peak occurring in Bed 6b (Fig. 3). The ratio then declines again before abruptly rising to peaks in the C. postbitteri postbitteri to C. dukouensis Zones and finally returns to pre-extinction levels in the upper C. dukouensis Zone.

Carbon and Mercury Isotopes

Our $\delta^{13}C_{carb}$ profile (Fig. 3) broadly tracks previous data (Wang et al., 2004; Jost et al., 2014). The $\delta^{13}C_{carb}$ increases from +3‰ to +5‰ during J. xuanhanensis–C.

hongshuiensis Zones, with a minor negative excursion (~0.5‰) in the upper J. granti Zone, before a major shift to lighter values occurred in the Lopingian C. postbitteri postbitteri–C. dukouensis Zones. MIF (Δ^{199}Hg) have negative values (–0.1‰ to –0.02‰) in the PLT reef and suddenly rise to positive values in Bed 5 after the termination of the reef, Δ^{199}Hg finally drop to negative values at the top of Bed 7 (Fig. 3). MDF (δ^{202}Hg) ranges from –1.34‰ to 0.15‰. Because MDF (δ^{202}Hg) can result from many physical, chemical and biological reactions, we do not interpret MDF (δ^{202}Hg) signatures here.

DISCUSSION

Reef Ecosystem Collapse, Benthos Turnover, and Proliferation of Microbiota

The PLT reef is composed of several microfacies suggesting the construction occurred over a spectrum of bathymetric and environmental conditions. This helps explain the high faunal diversity, because communities from many depths are recorded. Following reef collapse, hardground and peritidal facies (Beds 5–6) were developed. Of the reef biota, bryozoans are especially abundant but disappeared by the end-Guadalupian. The alatoconchids represent the youngest occurrence of this aberrant giant bivalve family, and their loss, along with the rugose corals, coincides with reef collapse. Most foraminiferal species disappeared prior to Bed 7, and the forms in Bed 6 are already dominated by post-extinction types. The turnover of pelagic fauna is clearly close to the GLB. The ammonoid turnover from goniatite- to ceratite-dominated faunas right at the earliest Lopingian (Ehiro and Shen, 2008). Conodonts also underwent a major turnover from Jinogondolella group to Clarkina group 20 cm below the GLB (Jin et al., 2006).

In addition, an coeval sponge reef has also been reported from the adjacent Tieqiao section in Laibin (Chen et al., 2009). Termination of reef development in both PLT and Tieqiao sections suggests the collapse of metazoan reefs prior to the GLB. The diversity of microbe-originated fossils in the Beds 5–6 is also noteworthy, indicating that the vacated ecospace lost by metazoan reef was immediately refilled by microbiota. Range data from the Laibin Limestone (Fig. 3) undoubtedly show a facies control on taxonomic occurrences near the GLB. In contrast, there is a turnover of pelagic elements (ammonoids and conodonts) around the GLB. Thus, biodiversity shows a stepwise depletion in the Laibin Limestone, suggesting a disconnection between benthic and pelagic crises.

Environment Perturbations

Two Hg spikes are recorded near the GLB in PLT (Fig. 3). The weak correlation between Hg and TOC concentrations (correlation test, P = 0.0138, estimate = –0.4066; R^2 = 0.12; Fig. DR4) suggests that the stratigraphic pattern of Hg concentration is not due to variation in TOC content. With respect to Hg sources, volcanic Hg has insignificant MIF (Δ^{199}Hg ≈0 ‰) (Thibodeau and Bergquist, 2017). Once emitted to the environment, MIF (Δ^{199}Hg) mostly occurs and results in positive Δ^{199}Hg values (Blum et al., 2014). In general, marine sediments that received $Hg^0_{(g)}$ through terrestrial runoff tend to have greater negative Δ^{199}Hg than atmospheric $Hg^0_{(g)}$, and terrestrial resources acquire negative Δ^{199}Hg values when plants and soils sequestrate $Hg^0_{(g)}$ (Thibodeau and Bergquist, 2017).

In PLT, two Hg spikes occur with sustained positive Δ^{199}Hg values (Fig. 3), indicating that sediments received Hg primarily through atmospheric Hg deposition. Thus, the observed Hg peaks are likely due to increased atmospheric mercury loading from a volcanic source. The termination age of ELIP (259.1 ± 0.5 Ma) is likely to be close to the age of GLB (Zhong et al., 2014), suggesting ELIP may be the Hg source. A notable positive Hg/TOC anomaly observed around the GLB in the Festningen section, Spitsbergen, (Grasby et al., 2016), has similar amplitude to the main Hg/TOC anomaly at PLT, suggesting that biotic changes at PLT are in response to a global phenomenon.

The positive Δ^{199}Hg shift is consistent with increased direct atmospheric deposition of volcanically derived Hg^{2+} to the ocean (Thibodeau and Bergquist, 2017). This shift also coincides with the reef demise, implying that onset of ELIP eruption, marked by increased Hg^{2+}, may have caused reef development to cease through significant CO_2 release triggering greenhouse warming, as seen in conodont oxygen isotopes record (Chen et al., 2011). Climate warming and elevated atmospheric nutrient flux may have then stimulated the post-extinction microbial proliferation. The large Hg/TOC peak in the C. postbitteri postbitteri to C. dukouensis Zones suggests intense eruptions in the earliest Lopingian, coincident with a negative δ^{13}C shift.

Emeishan magmas are estimated to have released nearly 5 Mt of SO_2 km^{-3} (Zhang et al., 2013), and the volume of the Emeishan basalts is at least 0.3×10^6 km^3 (Shellnutt, 2014). Thus, the total SO_2 release would be $>1.5 \times 10^6$ Mt, which corresponds to a total Hg input of >31.5 Mt to the atmosphere (assuming a Hg/SO_2 ratio of 0.21×10^{-4}; Nriagu, 1989). Major fluxes of volcanic Hg have been postulated as a possible extinction mechanism via poisoning of marine waters (Sanei et al., 2012). Marine anoxia is also seen in several locations around the world (Bond et al., 2015; Zhang et al., 2015; Wei et al., 2016) and is another potential cause of stress at this time. While the ELIP produced a global Hg record that, at PLT and Spitsbergen, is timed with a biotic crisis, further work in other regions is required to demonstrate global biotic impacts at this time.

CONCLUSIONS

The PLT provides a detailed record of major environmental and biotic changes in the GLB interval, here summarized into four stages:

1) A metazoan reef containing a high diversity of framework builders (bryozoans, Tubiphytes and corals) was developed prior to the GLB during a lowstand interval.

2) Two Hg/TOC anomalies occur either side of the GLB. The first, in the J. granti Zone, coincides with the collapse of the reef and the loss of several coral species and the alatoconchid bivalves. Positive Δ^{199}Hg values indicate this crisis is triggered by the eruption of ELIP volcanism with the effusion of volatiles causing the Hg/TOC peak.

3) The end-Guadalupian saw the proliferation of microbiotas that may have benefitted from climate warming and enhanced atmospheric nutrient input at this time.

4) Hg/TOC peaked in the earliest Lopingian, suggesting the acme of ELIP volcanism at this time. This coincided with rapid sea-level rise and deep-water anoxia, and a turnover amongst the pelagic biota which clearly post-dates the benthic crisis.

ACKNOWLEDGMENTS

We thank Pedro Marenco, Matthew Clapham and other anonymous reviewers for critical comments. This study was supported by NSFC grants (41572091, 41772007, 41661134047) and Hubei Provincial Natural Science Foundation grant (2017CFA019). It is a contribution to IGCP 630.

REFERENCES CITED

Blum, J., and Bergquist, B.A., 2007, Reporting of variations in the natural isotopic composition of mercury: Analytical and Bioanalytical Chemistry, v 388, p. 353–359, https://10.1007/s00216-007-1236-9.

Blum, J.D., Sherman, L.S., and Johnson, M.W., 2014, Mercury isotopes in Earth and environmental sciences: Annual Review of Earth and Planetary Sciences, v. 42, p. 249–269, https://doi.org/10.1146/annurev-earth-050212-124107.

Bond, D.P.G., Hilton, J., Wignall, P.B., Ali, J.R., Stevens, L.G., Sun, Y., and Lai, X., 2010, The Middle Permian (Capitanian) mass extinction on land and in the oceans:

Earth-Science Reviews, v. 102, p. 100–116, https://doi.org/10.1016/j.earscirev.2010.07.004.

Bond, D.P.G., Wignall, P.B., Joachimski, M.M., Sun, Y., Savov, I., Grasby, S.E., Beauchamp, B., and Blomeier, D.P.G., 2015, An abrupt extinction in the Middle Permian (Capitanian) of the Boreal Realm (Spitsbergen) and its link to anoxia and acidification: Geological Society of America Bulletin, v. 127, p. 1411–1421, https://doi.org/10.1130/B31216.1.

Chen, B., Joachimski, M.M., Sun, Y.D., Shem, S.Z., and Lai, X.L., 2011, Carbon and conodont apatite oxygen isotope records of Guadalupian-Lopingian boundary sections: Climatic or sea-level signal?: Palaeogeography, Palaeoclimatology, Palaeoecology, v. 311, p. 145–153, https://doi.org/10.1016/j.palaeo.2011.08.016.

Chen, Z.Q., George, A.D., and Yang, W.R., 2009, Effects of Middle-Late Permian sea-level changes and mass extinction on the formation of the Tieqiao skeletal mound in the Laibin area, South China: Australian Journal of Earth Sciences, v. 56, p. 745–763, http://dx.doi.org/10.1080/08120090903002581.

Ehiro, M., and Shen, S.Z., 2008, Permian ammonoid Kufengoceras from the uppermost Maokou Formation (Earliest Wuchiapingian) at Penglaitan, Laibin Area, Guangxi Autonomous Region, South China: Paleontological Research, v. 12, p. 255–259, https://doi.org/10.2517/1342-8144-12.3.255.

Gektidis, M., Dubinsky, Z., and Goffredo, S., 2007, Microendoliths of the shallow euphotic zone in open and shaded habitats at 30° N–Eilat, Israel–paleoecological implications: Facies, v. 53, p. 43–55, https://doi.org/10.1007/s10347-006-0091-z.

Grasby, S.E., Beauchamp, B., Bond, D.P.G., Wignall, P.B., and Sanei, H., 2016, Mercury anomalies associated with three extinction events (Capitanian crisis, latest Permian extinction and the Smithian/Spathian extinction) in NW Pangea: Geological Magazine, v. 153, p. 285–297, https://doi.org/10.1017/S0016756815000436.

Haq, B.U., and Schutter, S.R., 2008, A chronology of Paleozoic sea-level changes: Science, v. 322, p. 64–68, https://doi.org/10.1126/science.1161648.

Jin, Y.G., 1993, Pre-Lopingian benthos crisis: Comptes Rendus XII ICC-P, v. 2, p. 269–278.

Jin, Y.G., Shen, S.Z., Henderson, C.M., Wang, X., Wang, W., Wang, Y., Cao, C., and Shang, Q., 2006, The Global Stratotype Section and Point (GSSP) for the boundary between the Capitanian and Wuchiapingian stage (Permian): Episodes, v. 29, p. 253–262.

Jost, A.B., Mundil, R., He, B., Brown, S.T., Altiner, D., Sun, Y., DePaolo, D., and Payne, J.L., 2014, Constraining the cause of the end-Guadalupian extinction with coupled records of carbon and calcium isotopes: Earth and Planetary Science Letters, v. 396, p. 201–212, https://doi.org/10.1016/j.epsl.2014.04.014.

Nriagu, J.O., 1989, A global assessment of natural sources of atmospheric trace metals: Nature, v. 338, p. 47–49, https://doi.org/10.1038/338047a0.

Salama, W., EI-Kammar, A., Saunders, M., Morsy, R., and Kong, C., 2015, Microbial pathways and palaeoenvironmental conditions involved in the formation of phosphorite grains, Safaga District, Egypt: Sedimentary Geology, v. 325, p. 41–58, https://doi.org/10.1016/j.sedgeo.2015.05.004.

Sanei, H., Grasby, S.E., and Beauchamp, B., 2012, Latest Permian mercury anomalies: Geology, v. 40, p. 63–66, https://doi.org/10.1130/G32596.1.

Shellnutt, J.G., 2014, The Emeishan large igneous province: A synthesis: Geoscience Frontiers, v. 5, p. 369–394, https://doi.org/10.1016/j.gsf.2013.07.003.

Shen, S.Z., and Shi, G.R., 2009, Latest Guadalupian brachiopods from the Guadalupian/Lopingian boundary GSSP section at Penglaitan in Laibin, Guangxi, South China and implications for the timing of the pre-Lopingian crisis: Palaeoworld, v. 18, p. 152–161, https://doi.org/10.1016/j.palwor.2009.04.010.

Stanley, S., and Yang, X., 1994, A double mass extinction at the end of the Paleozoic era: Science, v. 266, p. 1340–1344, https://doi.org/10.1126/science.266.5189.1340.

Thibodeau, A.M., and Bergquist, B.A., 2017, Do mercury isotopes record the signature of massive volcanism in marine sedimentary records: Geology, v. 45, p. 95–96, https://doi.org/10.1130/focus012017.1.

Wang, W., Cao, C.Q., and Wang, Y., 2004, The carbon isotope excursion on GSSP candidate section of Lopingian-Guadalupian boundary: Earth and Planetary Science Letters, v. 220, p. 57–67, https://doi.org/10.1016/S0012-821X(04)00033-0.

Wei, H.Y., Wei, X., Qiu, Z., Song, H., and Shi, G., 2016, Redox conditions across the G–L boundary in South China: Evidence from pyrite morphology and sulfur isotopic compositions: Chemical Geology, v. 440, p. 1–14, https://doi.org/10.1016/j.chemgeo.2016.07.009.

Wignall, P.B., Védrine, S., Bond, D.P.G., Wang, W., Lai, X.L., Ali, J.R., and Jiang, H.S., 2009, Facies analysis and sea-level change at the Guadalupian–Lopingian Global Stratotype (Laibin, South China), and its bearing on the end-Guadalupian mass extinction: Journal of the Geological Society, v. 166, p. 655–666, https://doi.org/10.1144/0016-76492008-118.

Zhang, G., Zhang, X., Li, D., Farquhar, J., Shen, S., Chen, X., and Shen, Y.A., 2015, Widespread shoaling of sulfidic waters linked to the end-Guadalupian (Permian) mass extinction: Geology, v. 43, p. 1091–1094, https://doi.org/10.1130/g37284.1.

Zhang, Y., Ren, Z.Y., and Xu, Y.G., 2013, Sulfur in olivine-hosted melt inclusions from the Emeishan picrites: Implications for S degassing and its impact on environment: Journal of Geophysical Research. Solid Earth, v. 118, p. 4063–4070, https://doi.org/10.1002/jgrb.50324.

Zhong, Y.T., He, B., Mundil, R., and Xu, Y.G., 2014, CA-TIMS zircon U–Pb dating of felsic ignimbrite from the Binchuan section: Implications for the termination age of Emeishan large igneous province: Lithos, v. 204, p. 14–19, https://doi.org/10.1016/j.lithos.2014.03.005.

FIGURE CAPTIONS

Figure 1. (A) Paleogeographic map (R. Blakey: http://www2.nau.edu/rcb7/260moll.jpg) showing location of the PLT section (China). (B) G–L succession (Beds 1–7) of Penglaitan showing geometry of the reef and GLB position. The geologist, in red, is ~160 cm in height.

Figure 2. Selected PLT reef biota and microbiota. (A) Bryozoan-Tubiphytes framestone; (B) Encrusting networks of Fistulipora; (C) Coral Amplexocarinia sp.; (D) Eurygonum nodosum along the margins of a brachiopod shell. (E–F) Coccoid-like calcispheroid under microscope and SEM, (G) Ovummurus duoportius, (H–I) Bacterial clump-like spheroids under microscope and SEM, (J) Eurygonum nodosum on crinoid stem.

Figure 3. The PLT section showing: Covariations of microbiota, carbon isotopes (green open circle data from Wang et al. (2004), red triangle data from Jost et al. (2014), black,

solid circles: this study), Hg, TOC, Hg isotope, redox conditions (from Wei et al., 2016), sea-level changes, and stratigraphic distributions of fossils (Jin et al., 2006; Ehiro and Shen, 2008; Wignall et al. 2009; Shen and Shi, 2009; this study). Conodont zonation after Jin et al. (2006), Epo. = Epoch, Fm. = Formation, CZ = Conodont Zone, Lith. = Lithology, Rel. abu. = Relative abundance, C. h. = Clarkina hongshuiensis, C. po. = Clarkina postbitteri postbitteri, C. duk. = Clarkina dukouensis. u.s. = upper slope, l.s. = lower slope, ba. = basin. Relative abundances of Coccoid-like spheres (a), Bacterial clump-like spheres (b) and Ovummurus duoportius (c) are: few (<20 individuals /cm^2), common (20–50 individuals /cm^2), abundant (>50 individuals /cm^2), or areal percentages on 200 views (× 50) for Mastigocoleus testarum (d): few (<5%), common (5%–10%), and abundant (>10%).

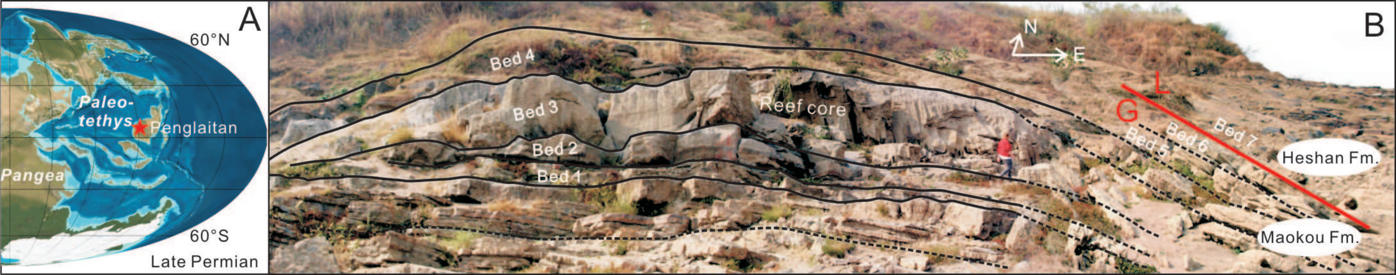
A
60°N
Paleo-tethys
Penglaitan
Pangea
60°S
Late Permian
B
N
E
Bed 4
Bed 3
Reef core
Bed 2
Bed 1
L
G
Bed 7
Bed 6
Bed 5
Heshan Fm.
Maokou Fm.

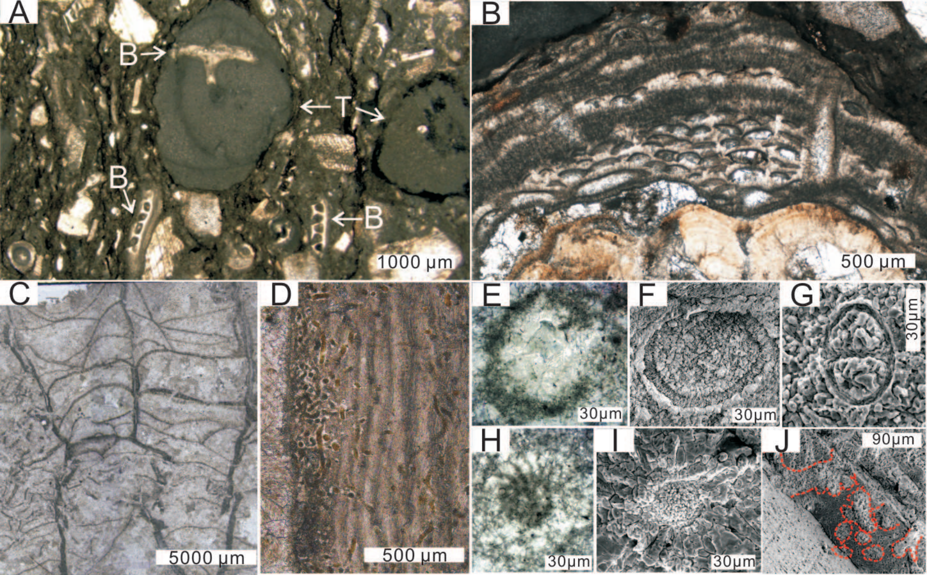
A
B
T
B
B
1000 µm
B
500 µm
C
5000 µm
D
500 µm
E
30µm
F
30µm
G
30µm
H
30µm
I
30µm
J
90µm

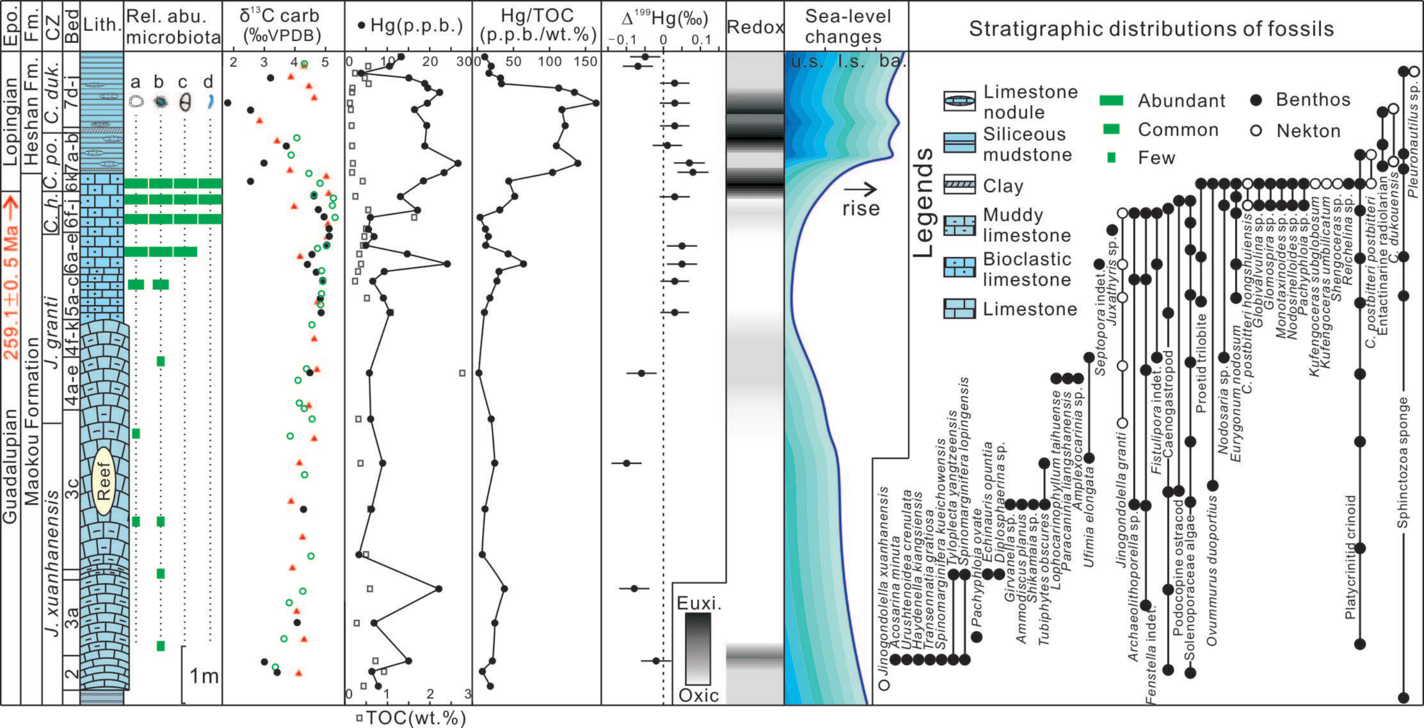
Epo.
Fm.
CZ
Bed
Lith.
Rel. abu. microbiota
δ13C carb (‰VPDB)
2 3 4 5
● Hg(p.p.b.)
0 10 20 30
Hg/TOC (p.p.b./wt.%)
0 50 100 150
Δ199Hg(‰)
−0.1 0 0.1
Redox
Sea-level changes
Stratigraphic distributions of fossils
Lopingian
Guadalupian
259.1±0.5 Ma →
Heshan Fm.
Maokou Formation
C. duk.
C. po.
C. h.
J. granti
J. xuanhanensis
7d-i
7a-b
6k
6f-i
6a-e
5a-c
4f-k
4a-e
3c
3a
2
Reef
1m
a
b
c
d
0 1 2 3
□ TOC(wt.%)
Euxi.
Oxic
u.s.
l.s.
ba.
→ rise
Legends
Limestone nodule
Siliceous mudstone
Clay
Muddy limestone
Bioclastic limestone
Limestone
Abundant
Common
Few
● Benthos
○ Nekton
Jinogondolella xuanhanensis
Acosarina minuta
Urushtenoidea crenulata
Haydenella kiangsiensis
Transennatia gratiosa
Spinomarginifera kueichowensis
Tyloplecta yangtzeensis
Spinomarginifera lopingensis
Pachyphloia ovata
Echinauris opuntia
Diplosphaerina sp.
Girvanella sp.
Ammodiscus planus
Shikamaia sp.
Tubiphytes obscures
Lophocarinophyllum taihuense
Paracaninia liangshanensis
Amplexocarinia sp.
Ufimia elongata
Septopora indet.
Juxathyris sp.
Jinogondolella granti
Archaeolithoporella sp.
Fenstella indet.
Fistulipora indet.
Caenogastropod
Podocopine ostracod
Solenoporaceae algae
Ovummurus duoportius
Proetid trilobite
Nodosaria sp.
Eurygonum nodosum
C. postbitteri hongshuiensis
Globivalvulina sp.
Glomospira sp.
Monotaxinoides sp.
Nodosinelloides sp.
Pachyphloia sp.
Kufengoceras subglobosum
Kufengoceras umbilicatum
Shengoceras sp.
Reichelina sp.
Platycrinitid crinoid
C. postbitteri postbitteri
Entactinarine radiolarian
C. dukouensis
Sphinctozoa sponge
Pleuronautilus sp.